UNSYS digital

Progress and Communication in Sciences

Conceptual Design of High-Resolution X-band Unmanned Aerial Vehicle (UAV) On-board Synthetic Aperture Radar

Heein Yang†, Good Fried Panggabean†, Agus Hendra†, Babag Purbantoro†, Cahya Edi Santosa†, Kaihei Namakura†, Yuta Izumi†, Josaphat Tetuko Sri Sumantyo†, and Kyeong-Rok Kim‡

†Chiba University, Center for Env. Remote Sensing (CEReS), Josaphat Microwave Remote Sensing Lab. (JMRSL), Japan

‡Department of Space Electronics and Information Technology, Ajou University, Korea

***Abstract*—**This paper presents the conceptual design of the unmanned aerial vehicle (UAV) on-board synthetic aperture radar (SAR) system. The SAR system is an active imaging sensor that uses microwave signal. The large scale UAV, JX-1 platform, is designed for land observation using SAR system. The proposed SAR system operates on X-band (8-10 GHz) with the bandwidth of 800 MHz and offers the high resolution images. The signal bandwidth defines the radar resolution, therefore, SAR system adopts the linearly frequency modulated (LFM) signal call chirp that is suitable for the wide bandwidth signal. In this paper, we implement the parallel direct digital frequency synthesizer (DDFS) chirp signal generator to generate the wide bandwidth signal with high stability using the field programmable gate array (FPGA). In addition, we analyze the specification, design constraints, and operational concepts of UAV. According to the operational concepts, we calculate the preliminary design parameters, geometry model, transmission signal properties, antenna design parameters, RF system parameters, and the signal-to-noise ratio (SNR). The contribution of this paper is the analysis on UAV operational concept, the design parameters of SAR system, the design of parallel DDFS chirp signal generator, and the verification of system design parameters for the realization of UAV on-board X-band high resolution SAR. The estimated spatial resolution of the proposed SAR system is 0.27 m by 0.23 m in range and azimuth directions, respectively.

***Keywords*—**Synthetic aperture radar, unmanned aerial vehicle, direct digital frequency synthesizer, radar system design.

I. Introduction

SYNTHETIC aperture radar (SAR) has been widely used in the field of remote sensing such as surveillance, land deformation research, urban managing, disaster monitoring, and etc [1]-[3]. It supports the high resolution images of target regardless of light and the weather condition. Usually, the SAR payload operates its mission on moving platforms such as satellite, unmanned aerial vehicle (UAV), airplane, and, car.

Generally, the resolution of radar system is inverse proportional to the signal bandwidth [4]. It indicates that the radar system with wider bandwidth can offer the higher resolution. In case of SAR, it transmits and receives microwave signal called chirp. The chirp signal is a kind of linearly frequency modulated (LFM) signal and its instantaneous frequency increases or decreases linearly with time. Therefore, the SAR supports the high resolution images of target by adopting the chirp signal.

There are several satellites or UAV on-board SARs on mission [5]-[9]. Because the SAR acquires the images on the move, the satellite on-board SARs usually operate its mission on the low-Earth orbit (LEO: 600-800 km). The satellite on-board SAR has several advantages on the stable operation, wide-area monitoring, and etc. However, the disadvantages also exist when the SAR is implemented on satellite platform. First, the performance of the space environment validated components such as maximum clock frequency is lower than commercial components. Second, tremendous time and budget costs are needed on system development. In general case, it takes approximately 5-year to develop and launch the satellite system. Third, the satellite has the revisit time and it takes around 14 days for a LEO satellite to visit same area. In this case, it takes long time to provide images within limited time.

To conduct the continuous and intensive monitoring on specific areas, the UAV on-board SAR is preferred target monitoring. Various UAV on-board SARs already exist in research fields and some of them are on practical mission. **Table I** shows the existing UAV on-board SAR systems [10]-[15].

The demands on UAV or plane on-board SAR are increasing because of its versatility to missions. In the meantime, the high performance and stability of SAR are also required. Therefore, the system optimizations as well as SAR system design techniques are important issues. When designing the UAV on-board SAR systems, there are several types of constraints to be considered such as the mountable payload size, the flight scenario of UAV, geometry between platform and target, power consumption, SAR system parameters, and etc.

Compared to the satellite platform, UAV on-board SAR generally performs its mission on 1-4 km above the ground and the mission on stratosphere (> 10 km) is being considered recently [16], [17]. The types of SAR systems can also be classified by microwave bands and each band has specific usage and characteristic. Among several microwave bands, the

Corresponding author: Heein Yang (email: kfcddong@gmail.com).
This paper was submitted on November 21, 2015; revised on December 5, 2015; and accepted on December 27, 2015.

TABLE I SPECIFICATION COMPARISON BETWEEN EXISTING UAV ON-BOARD SAR SYSTEMS

Payload	Platform	Mission altitude	Velocity	Center frequency	Bandwidth	Pulse width	Swath	Resolution
UAVSAR	Gulfstream III	13.8 km	100-250 m/s	1.26 GHz	80 MHz	5-50 us	16 km	
MiniSAR	Stemme S10 VT	1-2 km	61 m/s	9.75 GHz			> 2 km	< 0.5m
Lynx	IGNAT UAV	10 km	23.1 m/s					
AirMoss	Gulfstream III	12.5 km	100-250 m/s	280-400 MHz	20 MHz	5-50 us	7 km	7 m
NuSAR	Shadow 200	4.5 km	50-55 m/s	9.75 GHz				0.3 m
ARBRES-X	Polatus Porter	0.3 km	35 m/s	9.65 GHz	100 MHz		3.75 km	1.5 m

L (1-2 GHz), C (4-8 GHz), and X-band (8-10 GHz) are frequently used. L-band has relatively longer wavelength than other bands; approximately 23 cm. Due to its wavelength characteristic, L-band SAR is suitable for land deformation research, interferometry application, and resource exploration [18]. However, the frequency allocation of L-band for remote sensing is relatively narrow so that L-band SAR is not suitable for the high resolution imaging [4]. In addition, when designing the antennas, it requires relatively larger size than those of other bands. Because the UAV platform has rigid constraints on its payload size, the higher frequency bands are preferred for UAV on-board SAR.

Hence, X-band SAR system has been designed in this paper. The frequency of 800 MHz is allocated on X-band for remote sensing purpose. Therefore the X-band SAR is frequently used for high resolution imaging. Also to the properties of high frequency, the X-band antenna and RF system can be minimized.

Section II presents the design procedure of UAV on-board SAR system. The parallel direct digital frequency synthesizer (DDFS) for wideband chirp signal generator is proposed in Section III. In Section IV, the SAR system design parameters and simulation results are presented. This paper will conclude in Section V.

II. UAV ON-BOARD X-BAND SAR DESIGN AND ANALYSIS

This section presents the analysis on system requirements, the design procedure of SAR system, and comparison between existing UAV on-board SAR systems. The flow chart of system parameter design is presented in **Figure 1**. The SAR system design flow starts from requirements analysis. The analysis on antenna constraints will follow next and the geometry parameter can be calculated. Using the former parameters, we can calculate the pulse repetition frequency (PRF) and the resolution parameters that is the most important performance evaluation parameters. To transmit the appropriate signal to the target, the RF system properties should be considered. Finally, we evaluate the validity of the proposed SAR system using performance evaluation parameters. Several times of iteration are needed to satisfy the design requirements.

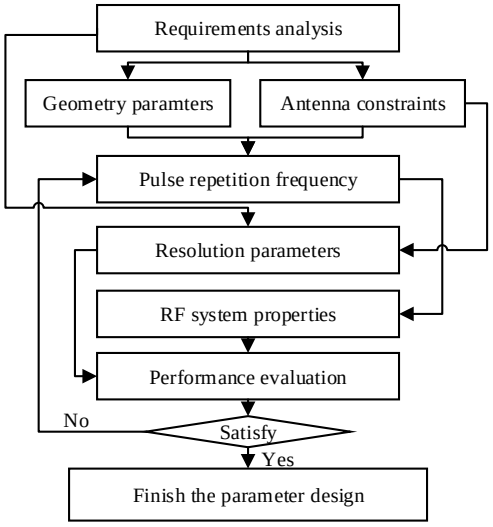

Figure 1 Flow chart of SAR system design parameters

A. Requirements analysis on mission concept

When designing the radar system, the designer first defines the scope and boundary of concepts and system requirements such as mission concepts and system requirements include the mission scenario, functional requirements, performance requirements, and etc. The first step of the UAV on-board SAR design is an analysis on platform specification. The proposed SAR system will be implemented on large scale UAV named JX-1. **Figure 2(a)** shows the structure of JX-1 [4], [16], [17]. It allows several measurement devices such as SAR system hyperspectral camera and for target imaging, the global navigation satellite system (GNSS) receiver and inertial measurement unit (IMU) sensors for position and attitude recording, the SAR image signal processing unit (ISP) for the on-board image processing, and etc.

Figure 2(b) and **(c)** show the front and bottom views of JX-1, respectively. The full wing span and the length of JX-1 are 6 m and 4.75 m. It consists of two main wings, one tail wing, one propeller using fuel motor, and etc. The mass of JX-1 by parts and brief specification are shown in **TABLE II** [16]. It can load the payload unit up to 25 kg and supports 20 liters of gasoline. The mission altitude is 1-4 km above the ground and cruising speed is 23 m/s.

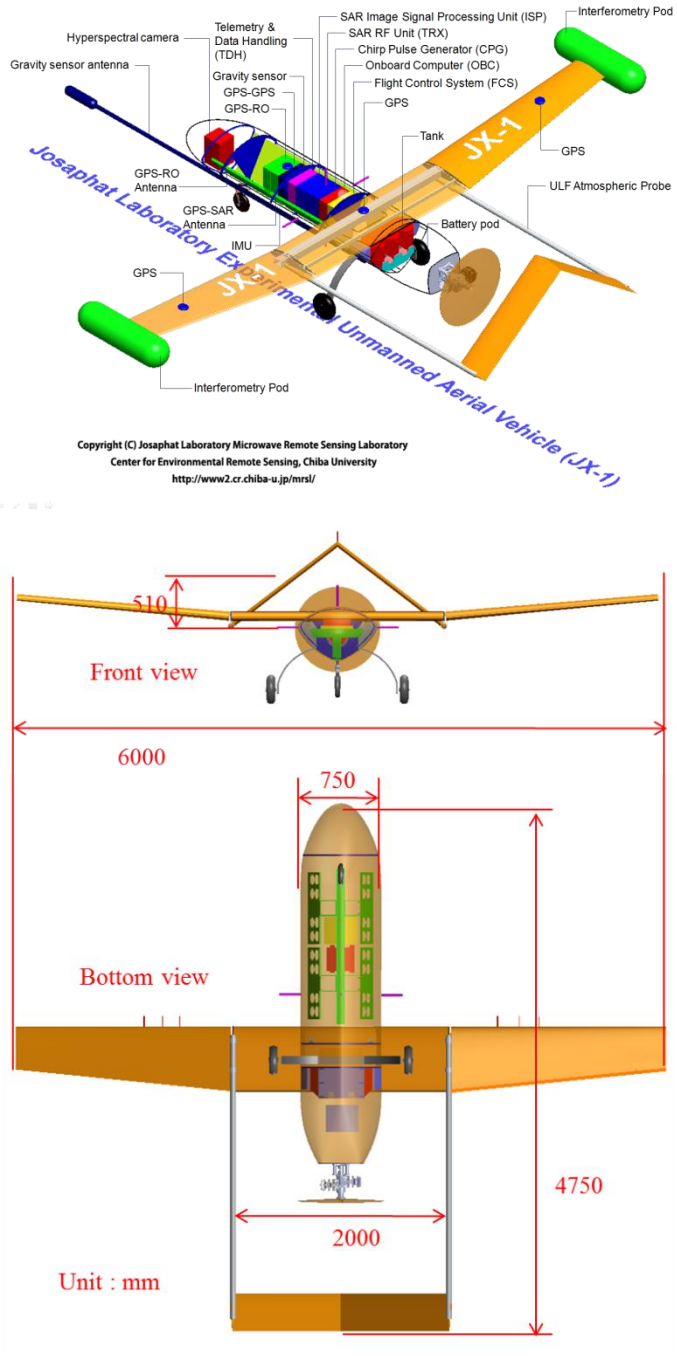

Figure 2 Structure of large scale UAV JX-1: (a) JX-1 payload operational concept; (b) front of view of JX-1; (c) bottom view of JX-1

The analysis on platform specification, the signal properties follow next. The slant range resolution of radar system is defined as,

$$\delta_{el} = \frac{c\tau}{2} = \frac{c}{2B}, \quad (1)$$

where c, τ, and B are the speed of light, pulse width, and bandwidth, respectively. In this paper, the center frequency and the signal bandwidth are set to 9.4 GHz and 800 MHz, respectively. In this case, the ideal slant range resolution will be 0.189 m. Compare to the existing UAV on-board SAR systems in **TABLE I**, the proposed SAR system has significantly higher resolution performance.

TABLE II SPECIFICATION OF JX-1

Weight of JX-1 hardware	
Items	**Weight (kg)**
Body (including battery, fuel tank, and etc.)	48.0
Center / main wing	16.0
Wing (2 unit x 10 kg ea.)	20.0
Ladder (2 unit x 7 kg ea.)	14.0
Other instruments	7.5
Gasoline (20 liters)	16.0
Payload (SAR system, IMU)	25.0
Total	146.5
Specification of JX-1	
Parameters	**Specification**
Mission altitude	1-4 km
Adjustable off nadir angle	40-60°
Maximum size of mountable antenna	
Elevation direction	0.4 m
Azimuth direction	1.5 m
Wing span	6 m
Platform length	4.75 m
Observation time	2.81-31.70 mins.

B. Analysis on antenna constraints

The transmission (Tx) and reception (Rx) antennas transmit and receive the microwave signal. In general, when assuming the planar antenna shape, the beam width of antenna has the relationship between wavelength and the length and width of antenna as,

$$\theta_{az} = 0.88\frac{\lambda}{L}, \theta_{el} = 0.88\frac{\lambda}{W}, \quad (2)$$

where θ_{az}, θ_{el}, λ, L, and W are the 3-dB aizmuth direction beam width, the 3-dB range direction beamwidth, wavelength, the length and width of antenna, respectively [1], [19]. The maximum mountable antenna size on JX-1 is 0.4 m x 1.5 m in elevation and azimuth directions, respectively. The proposed SAR system considers the full polarimetric antennas with two Tx antennas and two Rx antennas. The dimension of one unit of antenna is 150 mm by 400 mm in elevation and azimuth directions, respectively. Accoriding to the antenna size, the azimuth and range beam width can be calculated using (2). Several types of antenna exist for SAR system, however, the patched array antenna is considered in this paper. It has light weight and easy to instann and deploy.

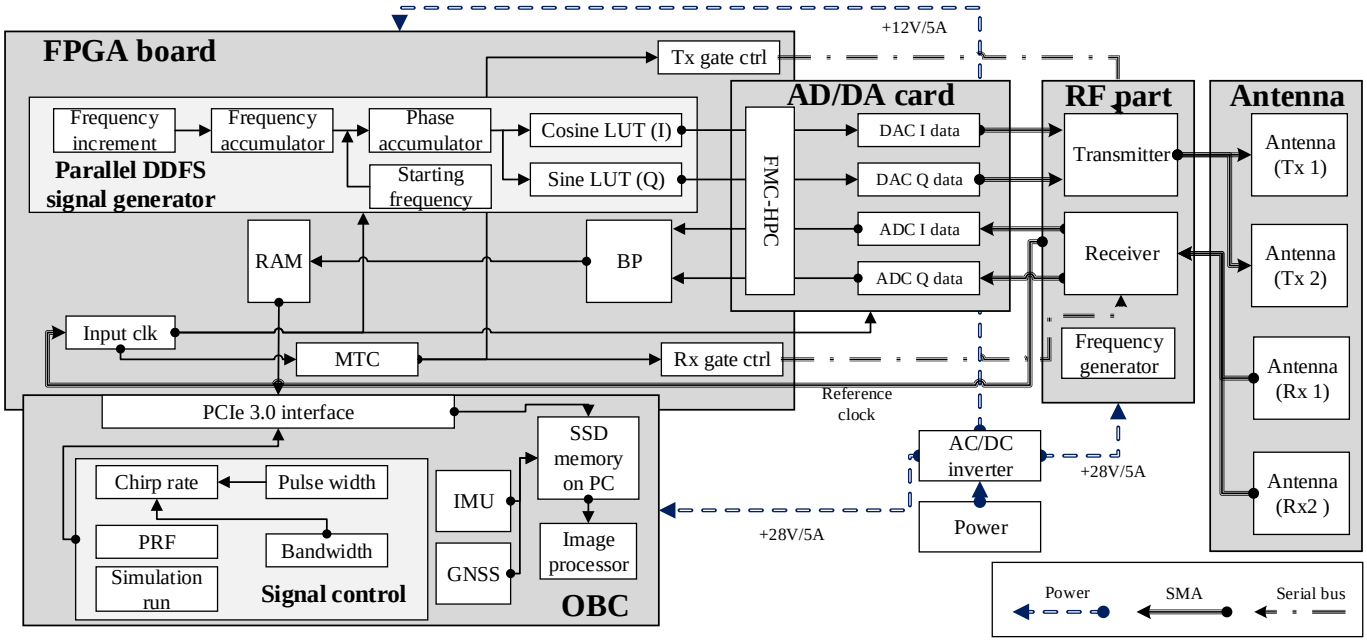

Figure 3 Block diagram of proposed X-band SAR system

C. Geometry parameters

The SAR has significantly different geometry characteristics compare to other radars or imaging sensors such as optical sensors, the visible near-infrared (VNIR) sensors, and etc. It adopts side-looking method that the radar observes perpendicular to the moving path but slightly tilted to the ground. Angle between the tilted antenna beam point and nadir point is called as off nadir angle. This paper, the SAR system on JX-1 platform adopts the off nadir angle of 45°. Considering the off nadir angle, the incidence angle to the ground (θ_i) can be derived as,

$$\theta_i = \sin^{-1}\left\{\frac{h \times \sin(\gamma_m)}{R_e}\right\}, \quad (3)$$

where, h, γ_m and R_e are the altitude of UAV, off nadir angle, and the Earth radius, respectively [1]. The ground swath (W_{gr}) and the synthetic aperture length (W_{az}) can be derived as,

$$W_{gr} = R_e \times \alpha_s, \quad (4)$$

$$W_{az} = 2\tan\left(\frac{\theta_{az}}{2}\right), \quad (5)$$

where, R_e and α_s are Earth radius and the core angle of swath points, respectively.

D. Pulse repetition frequency and resolution parameters

Generally, the frequency modulated continuous wave (FMCW) SAR is frequency used in UAV mission because of power consumption issues. However, the proposed SAR system adopts pulsed Doppler radar. A pulsed Doppler radar divides the Tx and Rx windows for signal acquisition. The collision between Tx and Rx signals during the mission distorts the received signal. To avoid from the problem, the SAR system has the valid range of PRF. The minimum and maximum PRFs are calculated as,

$$PRF_{min} = \frac{2v_{st}\sin(\theta_{az})}{c} f_c \approx \frac{2v_{st}\theta_{az}}{\lambda}, \quad (6)$$

$$PRF_{max} = \frac{1}{\left\lceil 2\tau + 2(R_f - R_n)/c \right\rceil}, \quad (7)$$

where, v_{st}, f_c, τ, R_f, and R_n are platform velocity, center frequency, pulse width, far range time, and near range time, respectively [1].

E. RF system properties and performance evaluation

RF system modulates the Tx chirp signal using mixer unit and up-converts Tx signal from base band to RF stage using high power amplifier (HPA). The RF system properties affect the performance of radar system, therefore, the system constraints such as peak power, maximum duty cycle, and system loss should be considered precisely.

The system performance can be evaluated using signal-to-noise ratio (SNR) and the noise-equivalent sigma zero (NESZ). The SNR can be expressed as,

$$SNR = \frac{P_{avg} A_{rx}^2 \eta^2 \delta_{el} \sigma^0}{8\pi R^3 k T_r \overline{NF} v_{st} \lambda L_s}, \quad (8)$$

where, P_{avg}, A_{rx}, η, σ^0, R, k, T_r, $\overline{NF}$, v_{st}, and L_s are the average power, receiver antenna gain, antenna efficiency,

NESZ, the distance to target, Plank constant, the absolute temperature of receiver, noise figure of system, platform velocity, and system loss, respectively.

NESZ of a SAR system indicates the radar cross section (RCS) level of noise. It differs from the purpose of SAR applications. In the case of forest and ocean observation, the NESZ can be set as -15 dB and -30 dB, respectively [20]-[22]. For example, a space-borne SAR sensor KOMPSAT-5 (KOrean Multi-Purpose SATllite-5) has the NESZ of -17 dB [23], [24]. In this paper, NESZ is set to -17 dB for urban land monitoring. System structure of the proposed X-band SAR system

F. System structure of the proposed X-band SAR system

The system structure of the proposed X-band SAR system is presented in figure 3. Proposed SAR system consists of the chirp signal generator on the field programmable gate array (FPGA), digital-to-analog and analog-to-digital card (AD/DA card), on-board computer (OBC), RF system, and antennas. The OBC unit consists of the SAR system controller that controls operation and commands. Also, it equips the IMU and GNSS units for attitude positioning.

The FPGA unit consists of the parallel DDFS chirp signal generator, mode and timing controller (MTC), and baseband processor (BP). The MTC defines the SAR observation modes and distributes the commands to RF system such as the control signals for Tx and Rx window gates. The BP stores the received signal from ADC to internal RAM unit and transmits the 8-bit digital data to OBC via PCIe 3.0 interface.

RF unit consists of Tx and Rx parts, frequency generator for up and down-conversion. As the X-band has high frequency, the IF stage up-conversion in I & Q modulator and the RF stage up-conversion in the high power amplifier (HPA) are considered.

III. Parallel DDFS Chirp Signal Generator

The chirp signal generator is one of the most important device in SAR systems. The bandwidth of chirp signal defines the slant resolution of SAR and the pulse width of chirp defines PRF. In order to achieve the system requirements, the digital system parts should be designed properly. This section presents the characteristics of chirp signal, the conventional DDFS chirp signal generator and the parallel DDFS chirp signal generator for high resolution imaging.

A. Characteristics of ideal chirp signal

The most significant characteristic of chirp signal is that its instantaneous frequency varied linearly with the time. The numerical expression of ideal chirp signal is shown as

$$s(t)=A(t)\exp\left(j\pi Kt^2\right), \tag{9}$$

where, t, $A(t)$, and K indicate the time variable, signal envelope, and the constant chirp rate, respectively. The signal envelope ($A(t)$) is defined as,

$$A(t)=1, \text{ where } -0.5\le t\le 0.5. \tag{10}$$

The phase and frequency of chirp signal from (9) are shown in (11) and (12), respectively.

$$f(t)=pKt^2, \tag{11}$$

$$f(t)=\frac{1}{2p}\frac{df(t)}{dt}=Kt. \tag{12}$$

From (11) and (12), we can notice the phase and frequency has the form of polynomial to the time [25], [26]. Also, (12) shows that instantaneous frequency of chirp varies linearly with K within time variable. Therefore, chirp signal can occupy the Kt [Hz] of bandwidth within the pulse width t and supports wide bandwidth by modifying the chirp rate K.

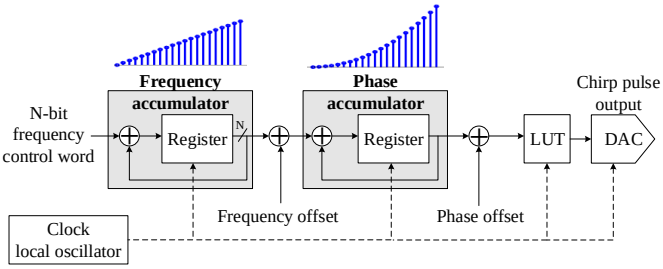

Figure 4 Block diagram of the conventional DDFS chirp signal generator

B. Conventional DDFS chirp signal generators

The DDFS is commonly used for digital chirp signal generator. It consists of registers that accumulate the input signal and look-up-tables (LUTs) that contains the amplitude value of sinusoid signal according to the phase address. The register unit in DDFS is called accumulator and it generates the phase of desired signal. Next, the phase signal output from accumulator is combined with the amplitude signal in LUT. **Figure 4** shows the simple block diagram of the conventional DDFS chirp signal generator [25], [27], [28].

The DDFS in figure 4 consists of two-set of accumulators and LUT. The N-bit input value is called frequency control word (FCW). The FCW is a constant binary value; therefore the output of frequency accumulator is a ramp-shape signal as depicted in **Figure 4**. Also, the output of phase accumulator is the second-order polynomial signal because the input signal is a ramp-shape signal. Using the accumulators, DDFS chirp signal generator can generate the second-order polynomial phase signal of chirp.

The behavior of the DDFS chirp signal generator can be derived using clock frequency, FCW, and bit-resolution. By notating the clock frequency as f_{clk}, the frequency increment and output frequency of DDFS can be defined as,

$$\Delta f=\frac{f_{\text{clk}}}{2^{\text{N}}}, \tag{13}$$

$$f_{\max}^{\text{DDFS}}=\Delta f\cdot \text{FCW}=\frac{f_{\text{clk}}\cdot \text{FCW}}{2^{\text{N}}}, \tag{14}$$

where Δf , $f_{\max}^{\mathrm{DDFS}}$, and N represent the frequency resolution, the maximum output frequency (or maximum bandwidth), and the bit resolution of DDFS system, respectively. The frequency resolution (Δf) indicates the number of clock within unit clock time (t_{clk}=($1/f_{clk}$)). The maximum frequency output of phase accumulator is multiplication between the frequency resolution and FCW. The maximum output frequency of DDFS depends on the clock frequency, FCW, and bit resolution of DDFS.

The numerical expression of DDFS chirp signal generator can be defined using FCW and N. In **Figure 4**, there are frequency accumulator and phase accumulator. Assuming that each accumulator unit continuously accumulates the input, each unit can be regarded as the integral operator with time. The input signal to frequency accumulator is FCW and its output signal with frequency offset can be defined as,

$$f_{\mathrm{DDFS}}(t)=\left(\frac{\mathrm{FCW}}{2^{\mathrm{N}}}\times t\right)+\frac{x_{\mathrm{f}}}{2^{\mathrm{N}}}, \tag{15}$$

where, x_f indicates the frequency offset value. In addition, the output signal of phase accumulator with phase offset is defined as,

$$\phi_{\mathrm{DDFS}}(t)=\left\{\frac{1}{2}\left(\frac{\mathrm{FCW}}{2^{\mathrm{N}}}\times t\right)^{2}+\left(\frac{x_{\mathrm{f}}}{2^{\mathrm{N}}}\times t\right)\right\}+\frac{x_{\mathrm{p}}}{2^{\mathrm{N}}}, \tag{16}$$

where, x_p presents the phase offset. Similar to the (11) and (12), the results of (15) and (16) are the functions of time *t*. The frequency offset and phase offset are used to adjust the starting value of frequency and phase. In the case of ideal chirp signal, the linear term ($x_f/2^N$)×t and random term ($x_p/2^N$) in (16) should be zero. Comparing the result between (11) and (16), the FCW input defines the chirp rate. The LUT synthesizes the phase output with amplitude value of sinusoid signal and generates the chirp signal with desired property.

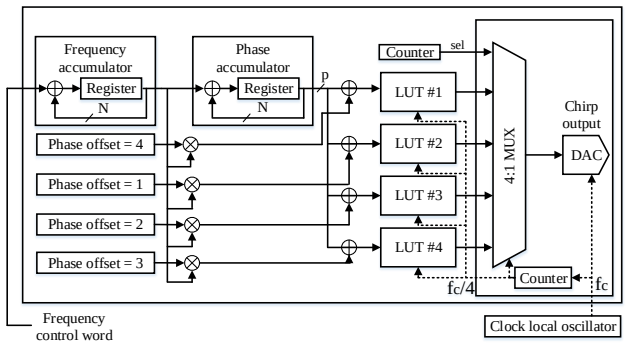

Figure 5 Block diagram of parallel DDFS chirp signal generator using 4 by 1 MUX

C. Parallel DDFS chirp signal generator

The common constraint of digital components is the limitation of clock frequency. The maximum bandwidth of the conventional DDFS chirp signal generator is also limited by the source clock frequency. Considering the Nyquist's theorem, the clock frequency should be at least two times larger than the desired bandwidth. Target system in this paper requires the bandwidth of 800 MHz, therefore the digital-to-analog converter (DAC) and analog-to-digital converter (ADC) require the clock frequency over than 1.6 GHz. However, the device with high clock frequency has budget and power consumption problems. The spectrum impurity such as spectral regrowth and spurious exist on every signal; however it gets severe when the clock frequency is not sufficient or the device is not stable.

To minimize the clock frequency problem, this paper proposes the parallel DDFS chirp signal generator shown in **Figure 5**. The proposed parallel DDFS consists of DDFS unit that generates the phase of chirp signal, 4-LUT in parallel, and 4-by-1 multiplexer (MUX) [27]. The parallel DDFS operates in sequential manner using the phase offset after the phase accumulator and the select counter that is an input to 4-by-1 MUX.

The advantage of the parallel DDFS chirp signal generator is the wide synthesizable frequency using relatively low clock frequency. Using the 4-by-1 MUX, each DDFS generates the phase every fourth sample of original phase signal. The discrete phase output of each DDFS of parallel DDFS ($\phi_{\mathrm{PDDFS}}[n]$) is shown in (17),

$$\phi_{\mathrm{PDDFS}}[n]=\begin{cases}\phi_{\mathrm{PDDFS}}^{\mathrm{i}=4}[n]=0,4^2k,8^2k,\cdots\\ \phi_{\mathrm{PDDFS}}^{\mathrm{i}=1}[n]=k,5^2k,9^2k,\cdots\\ \phi_{\mathrm{PDDFS}}^{\mathrm{i}=2}[n]=2k,6^2k,10^2k,\cdots\\ \phi_{PDDFS}^{\mathrm{i}=3}[n]=3k,7^2k,11^2k,\cdots\end{cases}, \tag{17}$$

where, i, *n*, and *k*, are the value of phase offset, the discrete clock number, and the frequency increment value (*k*=FCW/4), respectively [27], [29]-[31]. Each output enters LUT and finally MUX unit synthesizes the full-scale chirp signal. The maximum frequency of the parallel DDFS chirp signal generator ($f_{\max}^{\mathrm{PDDFS}}$) can be derived as,

$$f_{\max}^{\mathrm{PDDFS}}=\Delta f\cdot 4\cdot \mathrm{FCW}=\frac{4\cdot f_{\mathrm{clk}}\cdot \mathrm{FCW}}{2^{\mathrm{N}}}. \tag{18}$$

Comparing (14) and (18), The frequency output of parallel DDFS is four times larger than the conventional DDFS. Also, DDFS unit and LUTs are driven with the one-fourth of the clock frequency of clock local oscillator. By adopting the parallel DDFS, the chirp SAR system can support the wide bandwidth signal with stable clock condition. The chirp signal generator implemented on FPGA uses 10 MHz of reference clock from RF system and multiplies the reference clock up to 800 MHz using DCM module. In this case, each DDFS and LUTs of target device are driven by the 200 MHz of clock frequency. By using the parallel structure, the minimum required clock frequency for sampling can be. In addition, the spectrum characteristics such as ripple noise and attenuation can be improved.

TABLE II SAR SYSTEM DESIGN PARAMETERS FOR JX-1

Parameters	Values
Signal properties	
Center frequency (f_c)	9.4 GHz
Pulse width (τ_p)	1.5-15 μs
Bandwidth (BW)	800 MHz
Antenna constraints (Planar antenna)	
Antenna dimension	
Width (range direction)	150 mm
Length (azimuth direction)	400 mm
Beam width	
Range beam width	10.72°
Azimuth beam width	4.02°
Gain ($A_{tx} = A_{rx}$)	31.91 dBic
Antenna efficiency	0.7
Geometry parameters	
Altitude	1-4 km
Off nadir angle	45°
Incidence angle	45.21°
Ground swath	1.14 km
Range curvature	3.38 m
Pulse repetition frequency	
Minimum PRF	183.18 Hz
Maximum PRF	0.3 MHz
Operational PRF	1500 – 3580 Hz
Resolution parameters	
Range resolution	0.27 m
Azimuth resolution	0.23 m
RF system properties	
Peak power	50 W
Maximum duty cycle	4 %
System loss	10 dB
Performance evaluation	
NESZ	-17 dB
SNR	25 dB

TABLE III SAR SYSTEM DESIGN PARAMETERS FOR JX-1

Parameters	Ideal chirp	Conv. DDFS	Parallel DDFS	Enhancement
PSLR [dB]	-13.6995	-13.3589	-13.6677	-0.3088
ISLR [dB]	-10.1141	-12.2523	-10.0879	2.1644

IV. DESIGN AND SIMULATION RESULTS

This section presents the results of SAR system design parameters and simulation results of parallel DDFS chirp signal generator.

A. Results of SAR system design parameter

The SAR system design parameters are presented in table 3. Considering the JX-1 platform, the mission altitude, off nadir angle, are platform velocity are 1-4 km, 45°, and 23 m/s, respectively. To realize the small-sized high resolution SAR system, the center frequency and bandwidth are selected as 9.4 GHz and 800 MHz, respectively. Due to the characteristics of X-band, the antenna is also minimized as 150 mm by 400 mm. The expected performance of the proposed SAR system is the spatial resolution of 0.27 m by 0.23 m, the NESZ of -17 dB, and the SNR of 25 dB. The resolution parameters show that the proposed SAR system can support sub-meter class resolution. In addition, the NESZ and SNR also satisfy the requirements.

B. Simulation results of the proposed parallel DDFS

The proposed parallel DDFS is implemented on Xilinx FPGA boards and designed using Simulink and System generator from MATLAB and Xilinx. The target boards are Xilinx Virtex-5 ML555 FPGA board and MAXIM 19692 AD/DA card.

To verify the signal quality, the conventional DDFS and the proposed parallel DDFS chirp signal generators have been tested using its impulse response function (IRF). From the IRF, the peak-to-side lobe ratio (PSLR) and the integrated side lobe ratio (ISLR) can be investigated. The PSLR (I_{PSLR}) and ISLR (I_{ISLR}) can be derived as,

$$I_{PSLR} = I_{main}\left[\text{dB}\right] - I_{side}\left[\text{dB}\right] \quad (19)$$

$$I_{ISLR} = \frac{\int_{-1N}^{1N} \left|h(t)\right|^2 dt}{\int_{-10N}^{10N} \left|h(t)\right|^2 dt - \int_{-1N}^{1N} \left|h(t)\right|^2 dt} \quad (20)$$

where, I_{main}, I_{side}, h(t), and N are the peak value of main-lobe and side-lobe, the impulse response function, and number of lobe null, respectively [27], [32]-[35].

Figure 6(a) shows the comparison of PSLR and ISLR between the conventional DDFS and the proposed parallel DDFS chirp signal generators. The solid line with dot, dashed line, and solid line indicate the IRF of ideal chirp signal, conventional DDFS, and parallel DDFS, respectively. Compare to the conventional DDFS, the proposed parallel DDFS shows higher PSLR and it indicates that the parallel DDFS has lower noise level near the main-lobe. The comparison results of PSLR and ISLR are shown in table 4. The PSLR has been improved -0.3088 dB and it indicate the main-lobe of parallel DDFS is stronger to the side-lobe noise than the conventional DDFS chirp signal generator.

Figure 6(b) shows the spectrum between the conventional and parallel DDFSs. The dashed line and solid line present the spectrum of conventional and parallel DDFSs, respectively. Center frequency and bandwidth are 9.4 GHz and 800 MHz respectively. The spectrum of conventional DDFS degrades from the signal center and shows relatively larger ripple noise. Also, there is high out-band spur in the conventional DDFS spectrum due to the lack of sampling frequency. However, the parallel DDFS shows the flat spectrum characteristic in in-band. Also the ripple noise is smaller than former case. By driving the DDFS units parallel, the chirp signal generator can support the chirp signal of wide bandwidth with high-stability.

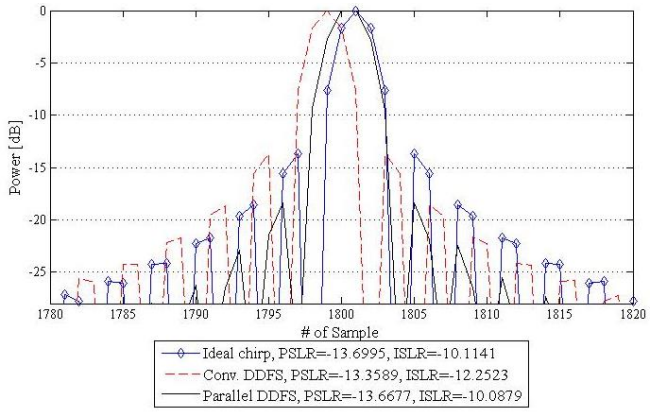

(a)

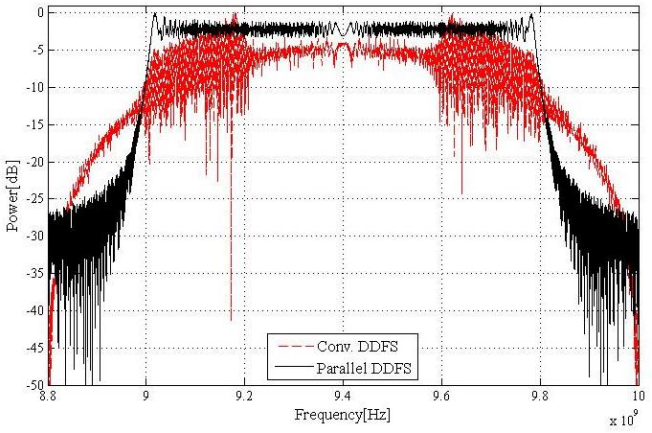

(b)

Figure 6: Comparison between conventional DDFS and parallel DDFS chirp signal generators: (a) IRF comparison using PSLR and ISLR; (b) spectrum characteristics comparison

V. Conclusion

Due to the all-weather radar characteristic, the demands SAR systems are gradually increasing all over the world. As presented in this paper, the satellites as well as UAV on-board SARs are on the development. The development trends are mainly focused on high-frequency SAR system because its payload size is smaller than those of lower frequency system (i e. antenna size) so that it can be implemented on UAV platforms.

A large scale UAV JX-1 is presented in this paper. JX-1 has larger space for payloads, therefore it can perform several mission in the same time. The main mission of JX-1 is land observation using SAR system. Hence, this paper presents the conceptual design of UAV on-board X-band SAR system: The design flow of SAR system, UAV specification, the preliminary SAR system design parameters, and the parallel DDFS chirp signal generators. According to the design results, the proposed JX-1 on-board X-band SAR can perform its mission 30 minutes in maximum and generate the approximately 1 km by 1 km image of target with the spatial resolution of 0.27 m by 0.23 m. The SAR system structure and parameter design results show that the proposed SAR system can offer the sub-meter class high resolution images from 1-4 km above the ground.

To support the high resolution imaging, the parallel DDFS chirp signal generator is adopted for signal generator. The parallel DDFS chirp signal generator operates on relatively lower clock frequency than the conventional single DDFS chirp signal generator. In addition, due to the sufficient clock frequency resource, the performance of parallel DDFS shows stable than those of the single DDFS chirp signal generator. The PSLR of parallel DDFS has been increased -0.3088 dB while ISLR has been decreased 2.1644 dB. The effect from ISLR decrement is negligibly small because the PSLR has the major effect on the receiver stage. In addition, the spectrum characteristic of parallel DDFS shows higher quality. The parallel DDFS chirp signal generator has flat spectrum, low ripple noise, and etc. while conventional DDFS chirp signal generator suffers from out-band spurious, large ripple noise, in-band attenuation. The simulation results indicate that the wide bandwidth chirp signal can be generated by using parallel DDFS and implemented on the high resolution SAR systems.

Acknowledgements

Josaphat Microwave Remote Sensing Laboratory (JMRSL) thanks to the Japanese Ministry of Education and Technology (Monbukagakusho); Japan International Cooperation Agency (JICA), Japan Science and Technology Agency (JST) for Science and Technology Research Partnership for Sustainable Development (SATREPS) Program, Weathernews, PASCO for TerraSAR-X images, JAXA for ALOS PALSAR and ALOS-2 PALSAR-2 images, National Institute for Environmental Studies (NIES) for ASTER images, GSI for GPS ground measurement data, Bhimasena, Chiba University – Venture Business Laboratory (VBL) etc for supporting JMRSL.

References

[1] K. Tomiyasu, "Tutorial review of synthetic-aperture radar (SAR) with applications to imaging of the ocean surface," *Proceedings of the IEEE*, Vol. 66, no. 5, pp. 563-583, 1978. CrossRef

[2] F. Argenti, A. Lapini, and L. Alparone, "A tutorial on speckle reduction in synthetic aperture radar images," *Geoscience and Remote Sensing Magazine, IEEE*, Vol. 1, no. 3, pp. 6-35, 2013. CrossRef

[3] H. Yang, D. G. Lee, T.-H. Kim, J. T. Sri Sumantyo, and J.-H. Kim, "Semi-automatic coastline extraction methos using synthetic aperture

radar images," *2014 IEEE 16th International Conference on Advanced Communication Tehonology (ICACT)*, pp. 678-681, Feb. 2014.

[4] Yohandri, V. Wissan, I. Firmansyah, P. Rizki Akbar, J. T. Sri Sumantyo, and H. Kuze, "Development of circuarly polarized array antenna for synthetic aperture radar sensor installed on UAV," *Progress In Electromagnetics Research C*, Vol. 19, pp. 119-133, 2011. CrossRef

[5] S.-R. Lee, "Overview of KOMPSAT-5 program, mission, and system,", *2010 IEEE International Geoscience and Remote Sensing Symposium (IGARSS)*, pp. 797-800, 2010. CrossRef

[6] M. Suess, S. Riegger, W. Pitz, and R. Werninghaus, "TerraSAR-X-design and performance," *in Proc. EUSAR*, Vol. 2, pp. 49-52, 2002.

[7] S. Buckreuss, W. Balzer, P. Muhlbauer, and R. Werninghaus, and W. Pitx, "The TerraSAR-X satellite project,", *2003 IEEE International Geoscience and Remote Sensing Symposium (IGARSS)*, pp. 3096-3098. CrossRef

[8] M. Virelli, A. Coletta, M. L. Battagliere, "ASI COSMO-SkyMed: Mission overview and data exploitation," *Geoscience and Remote Sensing Magazine, IEEE*, Vol. 2, no. 2, pp. 64-66, 2014. CrossRef

[9] M. Xing, X. Jiang, R. Wu, F. Zhou, and Z. Bao, "Motion compensation for UAV SAR based on raw radar data," *Geoscience and Remote Sensing, IEEE Transactions on*, IEEE, Vol. 47, no. 8, pp. 2870-2883, 2009.

[10] P. A. Rozen, S. Hensley, K. Wheeler, G. Sadowy, T. Miller, S. Shaffer, R. Muellerschoen, C. Jones, H. Zebker, and S. Madsen, "UAVSAR: a new NASA airborne SAR system for science and technology research," *2006 IEEE Conference on Radar*, pp. 22-29, 2006. CrossRef

[11] E. Chapin, A. Chau, J. Chen, B. Heavey, S. Hensley, Y. Lou, R. Machuzak, and M. Moghaddam, "AirMOSS: An Airborne P-band SAR to measure root-zone soil moisture," *2012 IEEE Conference on Radar*, pp. 693-698, 2012. CrossRef

[12] M. Edwards, D. Madsen, G. Stringham, A. Margulis, B. Wicks, and D. G. Long, "microASAR: A Small, Robust LFM-CW SAR for Operation on UAVs and Small Aircraft," *2008 IEEE International Geoscience and Remote Sensing Symposium (IGARSS)*, pp. 514-517, 2008. CrossRef

[13] P. Steeghs, E. V. Halsema, and P. Hoogeboom, "MINISAR: a Miniature, Lightweight, Low Cost, Scalable SAR System," *Proceeing of CEOS SAR Calibration/Validation Workshop'01*, pp. 125-128, 2011.

[14] W. Jian, L. Jin-mei, Y. Yuan, and F. Jun, "Research on application of unmanned aerial vehicles borne SAR," *2009 2nd IEEE Asian-Pacific Conference on Synthetic Aperture Radar (APSAR)*, pp. 60-63, 2009. CrossRef

[15] C. Bhattacharya, A. Roy, S. Navneet, A. Heddallikar, R. Pinto, "MicroSAR: Calibration of X-band high resolution FMCW synthetic aperture radar (SAR)," *2014 IEEE International Microwave and RF Confernece (IMARC)*, pp. 377-380, 2014.

[16] P. Rizki Akbar, J. R. Sri Sumantyo, V. C. Koo, and H. Kuze, "Estimation of Data Memory Capacity for Circularly Polarized Synthetic Aperture Radar onboard Unmanned Aerial Vehicle Platform (CP-SAR UAV)," *International Journal of Remote Sensing and Earth Sciences (IRESES)*, Vol. 7, pp. 24-35, 2010.

[17] H. Saito and J. T. Sri Sumantyo, "Synthetic Aperture Radar for UAVs and Small Satellite," *The IEICE Transactions of Communications*, Vol. J97-B, No. 11, pp. 992-998, 2014.

[18] Kankaku, Y. Osawa, Y. Suzuki, and T. Watanabe, "The overview of the L-band SAR onboard ALOS-2," *Proceedings of Progress in Electromagnetics Research Symposium (PIERS)*, pp. 735-738, Aug 2009.

[19] V. C. Koo, Y. K. Chan, G. Vetharatnam, M. Y. Chua, C. H. Lim, C.-S. Lim, C. C. Thum, T. S. Lim, Z. bin Ahmad, K. A. Mahmood, M. H. Bin Shahid, C. Y. Ang, W. Q. Tan, P. N. Tan, K. S. Yee, W. G. Cheaw, H. S. Boey, A. L. Choo, and B. C. Sew, "A new unmanned aerial vehicle synthetic aperture radar for environmental monitoring," *Progress in Electromagnetics Research*, Vol. 122, pp. 245-268, 2012. CrossRef

[20] L. C. Schroeder, D. H. Boggs, G. Dome, I. M. Halberstam, W. L. Jones, W. J. Pierson, and F. J. Wentz, "The relationship between wind vector and normalized radar cross section used to derive SEASAT-A satellite scatterometer winds," *Journal of Geophysical Research: Ocean (1978-2012)*, Vol. 81, pp. 3297-3317, 1982.

[21] M. Shimada, "Radiometric and geometric calibration of JERS-1 SAR," *Advances in Space Research*, Vol. 11, no. 1, pp. 79-88, 1996. CrossRef

[22] M. Shimada, "Long-term stability of L-band normalized radar cross section of Amazon rainforest using the JERS-1 SAR,", *Canadian Journal of Remote Sensing*, Vol. 31, no. 1, pp. 132-137, 2005. CrossRef

[23] J. Shin, K. Lee, and J. H. Kim, "Field test of KOMPSAT-5 calibration equipment," *2010 IEEE International Geoscience and Remote Sensing Symposium (IGARSS)*, pp. 805-807, 2010. CrossRef

[24] A. Moreira, P. Prats-Iraola, M. Younis, G. Krieger, I. Hajnsek, K. P. Papathanassiou, "A tutorial on synthetic aperture radar," *Geoscience Remote Sensing Magazing, IEEE*, Vol. 1, no. 1 pp. 6-43, 2013. CrossRef

[25] H. Yang, S. B. Ryu, H. C. Lee, S. G. Lee, S. S. Yong, and J.-H. Kim, "Implementation of DDS chirp signal generator on FPGA," *2014 IEEE International Conference on Information and Communication Technology Convergence*, pp. 956-959, Oct 2014. CrossRef

[26] H. Yang, J. H. An, H. W. Jung, and J.-H. Kim, "Circular polarization implementation on synthetic aperture radar," *2014 IEEE International Conference on Information and Communication Technology Convergence*, pp. 991-994, Oct 2014. CrossRef

[27] H. Yang, J. T. Sri Sumantyo, J. H. an, H. W. Jung, and J.-H. Kim, "Phase error compensation method using polynomial model for a direct digital synthezer based chirp signal generator," *2015 IEEE International Geoscience and Remote Sensing Symposium (IGARSS)*, pp. 786-789, Jul 2015. CrossRef

[28] J. H. An, H. W. Jung, H. Yang, S. B. Ryu, H. C. Lee, S. G. Lee, S. S. Yong, and J.-H. Kim, "Development of chirp signal generator for micro satellite on-board synthetic aperture radar," *2015 IEEE International Geoscience and Remote Sensing Symposium (IGARSS)*, pp. 3663-3666, Jul 2015. CrossRef

[29] W. Q. Wang, Q. Peng, and J. Cai, "Diversified MIMO SAR waveform analysis and generation," *2009 2nd IEEE Asian-Pacific Conference on Synthetic Aperture Radar (APSAR)*, pp. 270-273, 2009. CrossRef

[30] W. Q. Wang, Q. Peng, and J. Cai, "Waveform-diversity-based millimeter-wave UAV SAR remote sensing," *IEEE Transactions on Geoscience and Remote Sensing*, Vol. 47, no. 3, pp. 691-700, 2009. CrossRef

[31] N. Salerno, L. Simone, S. Cocchi, V. Viloni, M. Maffei, O. Cocciolollo, "Wideband arbitrary waveform generator for enhanced spaceborne SAR," *2008 IEEE European Radar Conference (EURAD)*, pp. 416-419, 2008.

[32] J.-B. Sung, S. Y. Kim, H. I. Lee, and B. T. Jeon, "Modeling and Simulation Techniques for Performance Analysis of High Resolution SAR System," *The Journal of Korean Institude of Electromagnetic Engineering and Science*, Vol. 24, no. 4, pp. 558-565, 2013. CrossRef

[33] J.-B. Sung, S. Y. Kim, H. I. Lee, and B. T. Jeon, "Development and Performance Compensation of the Extremely Stable Transceiver System for High Resolution Wideband Active Phased Array Synthetic Aperture Radar," *The Journal of Korean Institude of Electromagnetic Engineering and Science*, Vol. 21, no. 6, pp. 573-582, 2010. CrossRef

[34] S. Y. Kim and J. B. Sung, "Analysis on spectral regrowth of chirp bandwidth expansion technique in high-resolution SAR system," *Microwave and Optical Technology Letters*, Vol. 56, no. 2, pp. 400-403, 2014. CrossRef

[35] S. Y. Kim and N.-H. Myung, "Wideband linear frequency modulated waveform compensation using system predistortion and phase coefficients extraction method," *Microwave and Wireless Components Letters, IEEE*, Vol. 17, no. 11, pp. 808-810, 2007. CrossRef